

# Photoimaging with Color-Sensing Abilities by Tuning the Band Gap of a Single-Crystal Lead-Free Perovskite

Fa Cao, Xiaolei Deng, Xinya Liu, Li Su, Enliu Hong, Limin Wu,\* and Xiaosheng Fang\*



Cite This: *ACS Appl. Mater. Interfaces* 2023, 15, 28158–28165



Read Online

ACCESS |

Metrics & More

Article Recommendations

Supporting Information

**ABSTRACT:** Photodetectors (PDs) composed of lead-free metal halide perovskites have been a shining topic in optoelectronics. However, it is debatable whether perovskites are an n-type or p-type semiconductor with a direct or indirect band gap. Furthermore, to date, little research has been conducted on lead-free metal halide perovskites with color-sensing abilities. Herein, for the first time, single-crystal  $\text{MA}_3\text{Bi}_2\text{I}_{3x}\text{Br}_{9-3x}$  ( $x = 0, 1, 2$ , and  $3$ ) perovskites were systematically studied, and the results showed that  $\text{MA}_3\text{Bi}_2\text{I}_9$  is a p-type direct-band-gap semiconductor, whereas  $\text{MA}_3\text{Bi}_2\text{Br}_9$  is an n-type indirect-band-gap semiconductor. Furthermore, the band gap of  $\text{MA}_3\text{Bi}_2\text{I}_{3x}\text{Br}_{9-3x}$  ( $x = 0, 1, 2$ , and  $3$ ) perovskites can be systematically tuned from 2.06 to 2.55 eV, affording it with color-sensing abilities from 450 to 580 nm, respectively. The representative Au- $\text{MA}_3\text{Bi}_2\text{I}_9$ -ITO (ITO = indium tin oxide) PD exhibits a superior self-powered photodetecting performance with a high responsivity ( $15.8 \text{ mA W}^{-1}$ , 580 nm,  $1.0 \text{ mW cm}^{-2}$ ), detectivity ( $8.1 \times 10^{11} \text{ Jones}$ ), an on/off ratio (4231), LDR (72.5 dB) and a fast response speed (rise time of  $2 \mu\text{s}$  and decay time of  $29 \mu\text{s}$ ). This study not only facilitates the theoretical understanding of the band gap of perovskite materials but also sheds light on the application of lead-free perovskites in object interaction and color perception.

**KEYWORDS:** photoimaging, color-sensing, band-gap-tunable, lead-free perovskite,  $\text{MA}_3\text{Bi}_2\text{I}_{3x}\text{Br}_{9-3x}$  ( $x = 0, 1, 2$ , and  $3$ )

## 1. INTRODUCTION

With the development of modern society, automatic driving and object interaction play an increasingly important role in today's scientific and technological life.<sup>1,2</sup> Therefore, it is necessary to develop sensors with multiple functionalities to satisfy our daily demands. Photodetectors (PDs), as one of the most important sensors that can convert light signals to electric signals, have aroused great interest due to their applications in fields such as information exchange, space exploration, imaging, and so forth.<sup>3–5</sup> PDs with different functionalities have been well developed; for example, dual-band PDs have been fabricated for light communication, and ultraviolet (UV) PDs have been fabricated for imaging, issuing UV warnings, and wide-angle field-of-view cameras.<sup>6–8</sup> Yet, little research has been conducted on PDs with color-recognition abilities. Commercial Si PDs realized color-sensing abilities but require expensive filters or complex algorithms. Integration of various PDs with different light-sensitive materials and detecting capacities is a feasible way to realize color recognition.<sup>9</sup> Fortunately, metal halide perovskites can realize continuous adjustment of the band gap by adjusting the proportion of halogen atoms, demonstrating huge application prospects in color sensing.<sup>2,10</sup> For example, Sun et al. fabricated color-sensitive PDs by adjusting the proportion of halogen atoms in polycrystalline  $\text{MAPbI}_y\text{X}_{3-y}$  ( $\text{X} = \text{Cl}$  and  $\text{Br}$ ) perovskite thin films.<sup>9</sup> Mai et al. fabricated an interesting perovskite-based

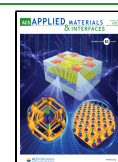
color camera, finding a pathway for the development of cameras and imitation of the natural eye.<sup>11</sup> However, the toxicity of Pb impedes the development of Pb-based perovskites. Therefore, environmentally friendly band-gap-tunable perovskites with color-sensing abilities are urgently needed.<sup>12</sup>

Among the possible elements that can be substituted for Pb in perovskites,  $\text{Bi}^{3+}$  exhibits the same electronic configuration as  $\text{Pb}^{2+}$ . Some emerging Bi-based perovskites and derivatives have been experimentally characterized and exhibit outstanding optoelectronic properties.<sup>13</sup> Our previous study reported that the  $\text{Cs}_3\text{Bi}_2\text{Br}_9/\text{Cs}_3\text{BiBr}_6$  perovskite-based bulk heterojunction demonstrates a self-powered photodetecting ability with an ultrahigh on/off ratio (18881) and a fast response speed (200 ns/1.09  $\mu\text{s}$ ).<sup>7</sup> Weak light ( $10 \text{ pW cm}^{-2}$ ) detection and imaging sensing applications were realized using self-powered  $\text{SnO}_2/\text{Cs}_3\text{BiI}_{10}$ .<sup>14</sup> While Bi-based perovskites have been developed for a long time, Bi-based perovskites still two controversial questions that need to be resolved:<sup>15</sup> (1)

Received: March 9, 2023

Accepted: May 16, 2023

Published: June 1, 2023



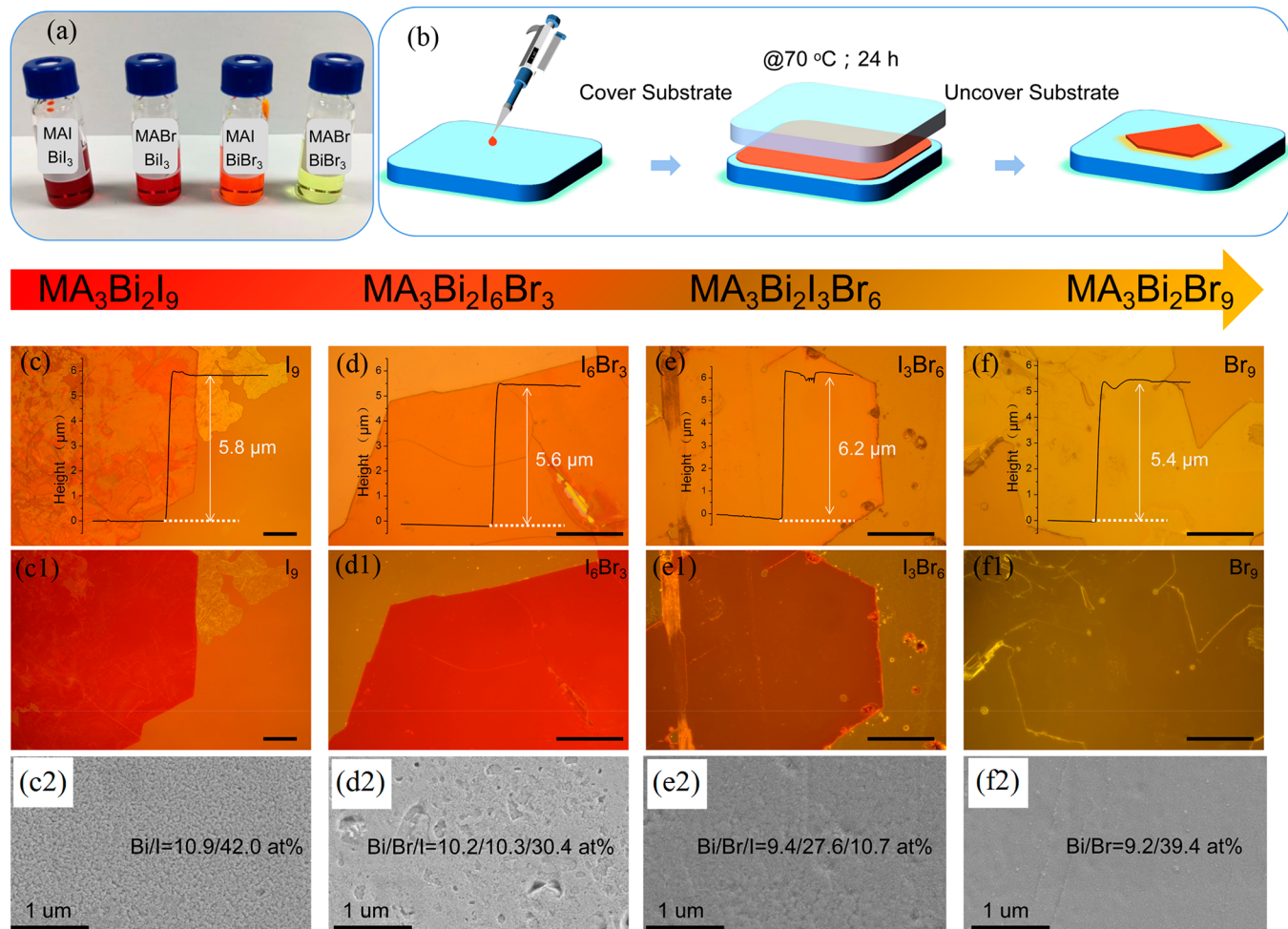


**Figure 1.** (a) Precursors and (b) fabrication process. (c1–f1) Bright- and dark-field optical microscopy images of MA<sub>3</sub>Bi<sub>2</sub>I<sub>9</sub>, MA<sub>3</sub>Bi<sub>2</sub>I<sub>6</sub>Br<sub>3</sub>, MA<sub>3</sub>Bi<sub>2</sub>I<sub>3</sub>Br<sub>6</sub>, and MA<sub>3</sub>Bi<sub>2</sub>Br<sub>9</sub>, respectively. The insets are height profiles of the corresponding microplates (scale bar = 200  $\mu$ m). (c2–f2) Corresponding SEM images. The insets are the atomic ratios of Bi, Br, and I.

Is a Bi-based perovskite an n-type semiconductor or a p-type semiconductor? (2) Does a Bi-based perovskite have a direct or an indirect band gap? Solving these two controversial questions can further guide the future development of high-performance perovskite PDs. Moreover, A<sub>3</sub>Bi<sub>2</sub>X<sub>9</sub> (A = Cs, MA, etc.; X = Cl, Br, and I) perovskites exhibit a series of outstanding photoelectrical properties and a band gap that can be tuned by changing the elements at the X site; therefore, A<sub>3</sub>Bi<sub>2</sub>X<sub>9</sub> (A = Cs, MA, etc.; X = Cl, Br, and I) perovskites satisfy our demand for color-sensing abilities.<sup>13,16</sup>

Herein, for the first time, single-crystal MA<sub>3</sub>Bi<sub>2</sub>I<sub>3x</sub>Br<sub>9-3x</sub> ( $x = 0, 1, 2$ , and 3) perovskites with color-sensing abilities (450–580 nm) were fabricated via a spatial confinement method. The results showed that MA<sub>3</sub>Bi<sub>2</sub>I<sub>9</sub> is a p-type direct-band-gap semiconductor, whereas MA<sub>3</sub>Bi<sub>2</sub>Br<sub>9</sub> is an n-type indirect-band-gap semiconductor. The energy band gap of MA<sub>3</sub>Bi<sub>2</sub>I<sub>3x</sub>Br<sub>9-3x</sub> ( $x = 0, 1, 2$ , and 3) perovskites can be systematically tuned from 2.06 to 2.55 eV by increasing the I content, allowing them to exhibit color-sensing abilities from 450 to 580 nm, respectively. The Au-MA<sub>3</sub>Bi<sub>2</sub>I<sub>9</sub>-ITO (ITO = indium tin oxide) PD exhibits a high self-powered responsivity (15.8 mA W<sup>-1</sup>; 580 nm; 1 mW cm<sup>-2</sup>), detectivity (8.1  $\times$  10<sup>11</sup> Jones), an on/off ratio (4231), LDR (72.5 dB), and a fast response speed (rise time = 2  $\mu$ s and decay time = 29  $\mu$ s). This study not only solves some controversial questions about Bi-based perovskites

but also shows the great application prospects of MA<sub>3</sub>Bi<sub>2</sub>I<sub>3x</sub>Br<sub>9-3x</sub> ( $x = 0, 1, 2$ , and 3) perovskites in object interaction and color perception.

## 2. EXPERIMENTAL SECTION

**2.1. Fabrication of MA<sub>3</sub>Bi<sub>2</sub>I<sub>3x</sub>Br<sub>9-3x</sub> ( $x = 0, 1, 2$ , and 3) on the Substrates.** 1.5  $\times$  1.5 cm glass/ITO substrates were sequentially cleaned with water and ethanol in an ultrasonic bath and dried with nitrogen. Before the growth process, 0.12 g of MAI (AlfaAesar Co., Ltd.; 99.7%) and 0.29 g of BiI<sub>3</sub> (AlfaAesar Co., Ltd.; 99%), 0.08 g of MABr (AlfaAesar Co., Ltd.; 99.7%) and 0.22 g of BiBr<sub>3</sub> (AlfaAesar Co., Ltd.; 99.7%), 0.12 g of MAI (AlfaAesar Co., Ltd.; 99.7%) and 0.22 g of BiBr<sub>3</sub> (AlfaAesar Co., Ltd.; 99%), and 0.08 g of MABr (AlfaAesar Co., Ltd.; 99.7%) and 0.29 g of BiI<sub>3</sub> (AlfaAesar Co., Ltd.; 99%) were mixed and dissolved in 1 mL of N,N-dimethylformamide (DMF, 99.8%) solvent, respectively, at room temperature to prepare the solutions. The solutions are shown in Figure 1a, with the color changing from dark red to light yellow (from MA<sub>3</sub>Bi<sub>2</sub>I<sub>9</sub> to MA<sub>3</sub>Bi<sub>2</sub>Br<sub>9</sub>). A total of 1  $\mu$ L of the solution was transferred to the center of the glass, which was covered by the target substrate. The growth temperature was maintained at 70 °C for 24 h. The detailed fabrication process is given in Figure 1b and our previous report.<sup>6</sup>

**2.2. Characterization of MA<sub>3</sub>Bi<sub>2</sub>I<sub>3x</sub>Br<sub>9-3x</sub> ( $x = 0, 1, 2$ , and 3).** The crystal phase, size, and morphology of MA<sub>3</sub>Bi<sub>2</sub>I<sub>3x</sub>Br<sub>9-3x</sub> ( $x = 0, 1, 2$ , and 3) were determined via X-ray diffraction (XRD; Cu K $\alpha$  radiation source,  $\lambda = 0.15418$  nm), optical microscopy (Olympus), field-emission scanning electron microscopy (SEM; FEI Nova

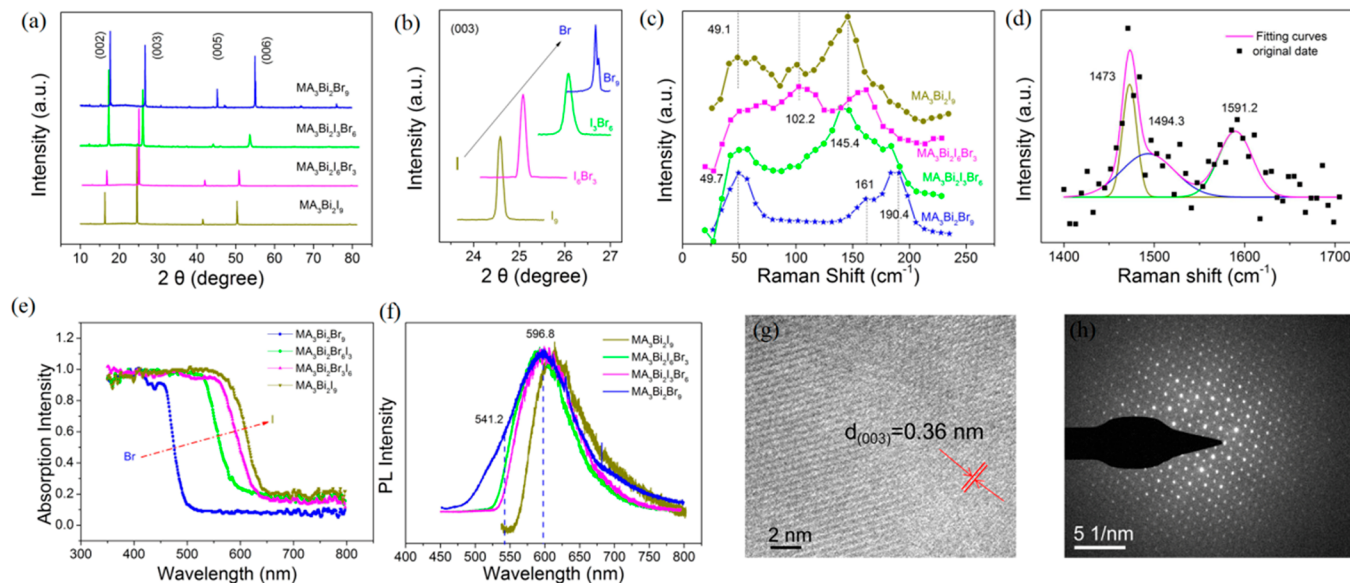


**Figure 2.** (a) XRD patterns of perovskite  $\text{MA}_3\text{Bi}_2\text{I}_{3x}\text{Br}_{9-3x}$  ( $x = 0, 1, 2$ , and  $3$ ) microplates. (b) Enlarged view of the corresponding (003) planes showing a continuous shift to higher Bragg angles with an increase in the Br proportion. (c and d) Raman spectra of the  $\text{MA}_3\text{Bi}_2\text{I}_{3x}\text{Br}_{9-3x}$  ( $x = 0, 1, 2$ , and  $3$ ) microplates. (e) Absorption spectra of  $\text{MA}_3\text{Bi}_2\text{I}_{3x}\text{Br}_{9-3x}$  ( $x = 0, 1, 2$ , and  $3$ ). (f) PL emissions of the  $\text{MA}_3\text{Bi}_2\text{I}_{3x}\text{Br}_{9-3x}$  ( $x = 0, 1, 2$ , and  $3$ ) microplates. (g and h) HRTEM images and corresponding SAED patterns of  $\text{MA}_3\text{Bi}_2\text{I}_9$ .

NanoSEM 430), and transmission electron microscopy (TEM; JEOL JEM-2100F). The thickness of  $\text{MA}_3\text{Bi}_2\text{I}_{3x}\text{Br}_{9-3x}$  was measured using a Step Profiler. The elemental information on  $\text{MA}_3\text{Bi}_2\text{I}_{3x}\text{Br}_{9-3x}$  was collected via X-ray photoelectron spectroscopy (XPS; Thermo Fisher ESCALAB 250; Al K $\alpha$  X-ray radiation) and energy-dispersive X-ray spectroscopy (EDS). Raman measurement and photoluminescent tests were performed using Raman microscopy and photoluminescence (excitation wavelength = 325 and 532 nm). Focused-ion-beam measurements were performed using an FEI Strata 400S.

**2.3. Fabrication of PDs.** Commercially purchased Cu grids (300 mesh, with the square voids of 50- $\mu\text{m}$  side length) were placed on top of the  $\text{MA}_3\text{Bi}_2\text{I}_{3x}\text{Br}_{9-3x}$  microplates. Next, Au electrodes ( $\sim 50$  nm) were thermally evaporated onto the sample. After removal of the Cu grids, square-shaped electrodes that were  $\sim 20$ - $\mu\text{m}$  apart were successfully formed on the  $\text{MA}_3\text{Bi}_2\text{I}_{3x}\text{Br}_{9-3x}$  microplates. Here, four kinds of PDs were fabricated, namely, Au- $\text{MA}_3\text{Bi}_2\text{I}_9$ -Au (PD1), Au- $\text{MA}_3\text{Bi}_2\text{I}_6\text{Br}_3$ -Au (PD2), Au- $\text{MA}_3\text{Bi}_2\text{I}_3\text{Br}_6$ -Au (PD3), and Au- $\text{MA}_3\text{Bi}_2\text{Br}_9$ -Au (PD4).

**2.4. Photoelectric Measurements of  $\text{MA}_3\text{Bi}_2\text{I}_{3x}\text{Br}_{9-3x}$  ( $x = 0, 1, 2$ , and  $3$ ).** All of the PD measurements were performed using a standard four-probe station with a Keithley 4200S semiconductor analyzer coupled with a 450 W Xe lamp equipped with a monochromator as the light source. Moreover, a 355 nm Q-switch Nd:YAG laser and an oscilloscope (Tektronix MSO/DPO5000) were used to record the transient photoresponse.

Responsivity ( $R$ ) and detectivity ( $D^*$ ) were used to evaluate the performance ( $R = \frac{I_l - I_d}{P_A}$ , where  $I_l$  is the light current,  $I_d$  is the dark current,  $P$  is the power density, and  $A$  is the effective light area, and  $D^* = \frac{R}{(2eI_d/A)^{1/2}}$ , where  $e = 1.6 \times 10^{-19} \text{ C}$ ).  $R$  denotes how efficiently a PD responds to an optical signal, and  $D^*$  means the ability to detect weak signals from a noisy environment. The LDR is the range of incident light power in which a PD responds linearly to external illumination.<sup>17</sup> Moreover, LDR can be calculated using  $\text{LDR} (\text{dB}) = 20 \log \left( \frac{I_l}{I_d} \right)$ , where  $I_l$  is the light current obtained at a light intensity of  $1.0 \text{ mW cm}^{-2}$ .<sup>4</sup> The rise and decay times are defined as the time for the current to increase to 90% of its maximum after exposure to incident light and the time for the current to decrease to 10% of its maximum after removal of the incident light.

**2.5. Electronic Structure Calculation.** All theoretical calculations were performed using the density functional theory (DFT) method, as implemented in the Vienna Ab Initio Simulation Package. The electron-ion interaction was described using the projector-augmented-wave method, and the electron exchange and correlation energies were solved within the generalized gradient approximation using the Perdew–Burke–Ernzerhof exchange-correlation functional.<sup>18–20</sup> The kinetic energy cutoff of the plane wave was 500 eV, and the convergence criterion for the residual forces and total energies were  $0.03 \text{ eV } \text{\AA}^{-1}$  and  $10^{-5} \text{ eV}$ , respectively. A  $3 \times 3 \times 1$  Monkhorst–Pack  $k$ -point grid was used to sample the Brillouin zone.

### 3. RESULTS AND DISCUSSION

All of the precursors and their detailed fabrication processes are shown in Figure 1a,b. Parts c–f of Figure 1 display the bright-field optical microscopy images of  $\text{MA}_3\text{Bi}_2\text{I}_9$ ,  $\text{MA}_3\text{Bi}_2\text{I}_6\text{Br}_3$ ,  $\text{MA}_3\text{Bi}_2\text{I}_3\text{Br}_6$ , and  $\text{MA}_3\text{Bi}_2\text{Br}_9$ , respectively, and their insets are the corresponding height profiles of the corresponding microplates. The average diameter of  $\text{MA}_3\text{Bi}_2\text{I}_9$  is about  $\sim 600 \mu\text{m}$ , which is larger than that of  $\text{MA}_3\text{Bi}_2\text{I}_6\text{Br}_3$ ,  $\text{MA}_3\text{Bi}_2\text{I}_3\text{Br}_6$ , and  $\text{MA}_3\text{Bi}_2\text{Br}_9$  ( $\sim 450 \mu\text{m}$ ). Meanwhile, all  $\text{MA}_3\text{Bi}_2\text{I}_{3x}\text{Br}_{9-3x}$  ( $x = 0, 1, 2$ , and  $3$ ) microplates show almost the same thickness of approximately  $5.4$ – $6.2 \mu\text{m}$ , while the dark-field optical microscopy images (Figure 1c1–f1) show that the color of the microplates changes from dark red to light yellow when the components changed from I to Br. The color difference in dark-field optical microscopy image is caused by a change of the semiconductor band gap. SEM was further employed to study the surface micromorphology of the microplates, as shown in Figures 1c2–f2. The results show that  $\text{MA}_3\text{Bi}_2\text{I}_9$  and  $\text{MA}_3\text{Bi}_2\text{Br}_9$  are smoother than  $\text{MA}_3\text{Bi}_2\text{I}_6\text{Br}_3$  and  $\text{MA}_3\text{Bi}_2\text{I}_3\text{Br}_6$  probably because the doping of I in  $\text{MA}_3\text{Bi}_2\text{Br}_9$  or Br in  $\text{MA}_3\text{Bi}_2\text{I}_9$  introduces defects in the microplates. The EDS mappings of  $\text{MA}_3\text{Bi}_2\text{I}_{3x}\text{Br}_{9-3x}$  ( $x = 0, 1, 2$ , and  $3$ ; Figure S1) further demonstrate the uniform distribution of C, N, Bi, Br, and I. The atom ratios of Bi, Br, and I are about 10.9:0.42, 10.2:10.3:30.4, 9.4:27.6:10.7, and 9.2:0:39.4 for  $\text{MA}_3\text{Bi}_2\text{I}_9$ ,  $\text{MA}_3\text{Bi}_2\text{I}_6\text{Br}_3$ ,  $\text{MA}_3\text{Bi}_2\text{I}_3\text{Br}_6$ , and  $\text{MA}_3\text{Bi}_2\text{Br}_9$ , respectively. So, we can confirm that the

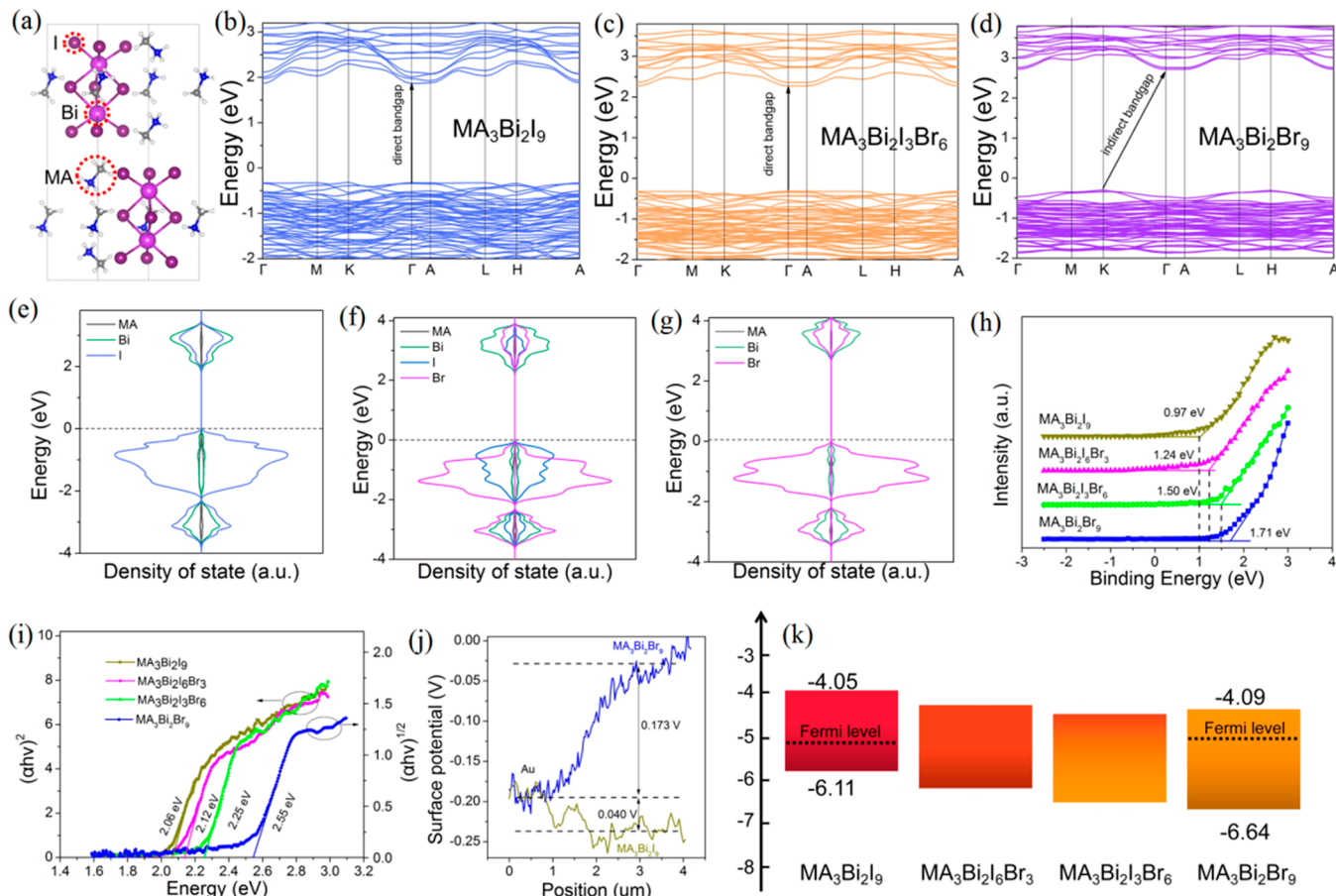


**Figure 3.** (a) Crystal-structure model of  $\text{MA}_3\text{Bi}_2\text{I}_9$ . (b–d) Band structures and (e–g) corresponding DOSs of  $\text{MA}_3\text{Bi}_2\text{I}_9$ ,  $\text{MA}_3\text{Bi}_2\text{I}_3\text{Br}_6$ , and  $\text{MA}_3\text{Bi}_2\text{Br}_9$ . (h and i) VB spectra and energy band gaps of the  $\text{MA}_3\text{Bi}_2\text{I}_{3x}\text{Br}_{9-3x}$  ( $x = 0, 1, 2$ , and  $3$ ) microplates. (j) KPFM spectra of  $\text{MA}_3\text{Bi}_2\text{I}_9$  and  $\text{MA}_3\text{Bi}_2\text{Br}_9$ . (k) Energy band alignments of  $\text{MA}_3\text{Bi}_2\text{I}_{3x}\text{Br}_{9-3x}$  ( $x = 0, 1, 2$ , and  $3$ ).

microplates are formed according to the ratio of MAI, MABr,  $\text{BiI}_3$ , and  $\text{BiBr}_3$  raw materials; that is, a Bi-based perovskite with any proportion of I and Br can be obtained by adjusting the ratio of the raw materials.

The change in the XRD peak positions of  $\text{MA}_3\text{Bi}_2\text{I}_{3x}\text{Br}_{9-3x}$  ( $x = 0, 1, 2$ , and  $3$ ) microplates with halide substitution was also studied, as shown in Figure 2a. All  $\text{MA}_3\text{Bi}_2\text{I}_{3x}\text{Br}_{9-3x}$  microplates exhibit high growth in the (001) direction, and the XRD profiles of  $\text{MA}_3\text{Bi}_2\text{I}_{3x}\text{Br}_{9-3x}$  microplates also exhibit clear (002), (003), (005), and (006) peaks.<sup>21,22</sup> The enlarged views of the (003) peaks (Figure 2b) show that, as the Br content in  $\text{MA}_3\text{Bi}_2\text{I}_{3x}\text{Br}_{9-3x}$  increases, the characteristic (003) diffraction peaks gradually shift to higher  $2\theta$  values (from  $24.58^\circ$  to  $26.68^\circ$ ). According to the Bragg diffraction equation  $2d \sin \theta = n\lambda$ , the atomic radius of Br was smaller than that of I, which caused a shift to higher  $2\theta$  values with an increase in the Br content. Raman microanalysis was further employed to obtain local structure information (Figure 2c). The two Raman peaks centered at  $190.4$  and  $161\text{ cm}^{-1}$  are assigned to the Bi–Br stretching modes of  $\text{MA}_3\text{Bi}_2\text{Br}_9$ .<sup>22</sup> As the I content increases, they gradually disappeared, and new peaks at  $145.4$  and  $102.2\text{ cm}^{-1}$  can be assigned to the Bi–I stretching modes of  $\text{MA}_3\text{Bi}_2\text{I}_9$ . The peaks at  $1473\text{ cm}^{-1}$  in the Raman spectra can be assigned to  $\text{CH}_3$  stretching modes, whereas those at  $1494.3$  and  $1591.2\text{ cm}^{-1}$  can be assigned to the  $\text{NH}_3$  stretching modes, as shown in Figure 2d.<sup>23</sup> The chemical composition of  $\text{MA}_3\text{Bi}_2\text{I}_3\text{Br}_6$  was further investigated by XPS, as shown in

Figure S2. The chemicals of C, N, Bi, I, and Br can clearly be seen, and no other impurities can be found in the microplates. Figure S2a shows the C 1s XPS spectrum fitted by two peaks at  $284.5$  eV (absorbed C) and  $285.6$  eV ( $\text{CH}_3$  bonding), respectively. The N 1s XPS peak is centered at  $401.7$  eV (Figure S2b), which can be attributed to N–H bonding. The Bi  $4f_{7/2}$  ( $159.0$  eV) and  $4f_{5/2}$  ( $164.3$  eV), Br  $3d_{5/2}$  ( $68.1$  eV) and Br  $3d_{3/2}$  ( $69.2$  eV), and I  $3d_{5/2}$  ( $618.9$  eV) and I  $3d_{3/2}$  ( $630.4$  eV) peaks, indicating that the valences of Bi, Br, and I are  $3+$ ,  $1-$ , and  $1-$ , respectively, as shown in Figure S2c–e, are consistent with the formula.<sup>24</sup> The optical properties of the as-synthesized  $\text{MA}_3\text{Bi}_2\text{I}_{3x}\text{Br}_{9-3x}$  ( $x = 0, 1, 2$ , and  $3$ ) microplates were studied by UV-visible absorption and photoluminescence (PL) emission spectroscopy. As shown in Figure 2e, the absorption peaks of  $\text{MA}_3\text{Bi}_2\text{I}_9$ ,  $\text{MA}_3\text{Bi}_2\text{I}_6\text{Br}_3$ ,  $\text{MA}_3\text{Bi}_2\text{I}_3\text{Br}_6$ , and  $\text{MA}_3\text{Bi}_2\text{Br}_9$  are observed at  $580$ ,  $550$ ,  $530$ , and  $450$  nm, respectively, obviously red shifting with an increase in the I content, suggesting a decrease in the band gap, which can be further proven by a color change in the dark-field optical microscopy images. Figure 2f shows the PL emission of the  $\text{MA}_3\text{Bi}_2\text{I}_{3x}\text{Br}_{9-3x}$  ( $x = 0, 1, 2$ , and  $3$ ) microplates. The near-band-edge (NBE) PL emission of  $\text{MA}_3\text{Bi}_2\text{I}_9$  is observed at  $614.8$  nm,<sup>22</sup> and with Br doping, the NBE PL emissions of  $\text{MA}_3\text{Bi}_2\text{I}_6\text{Br}_3$  and  $\text{MA}_3\text{Bi}_2\text{I}_3\text{Br}_6$  shift to  $592$  nm. Interestingly, the PL emission of  $\text{MA}_3\text{Bi}_2\text{Br}_9$  can be fitted by two peaks centered at  $541.2$  and  $596.8$  nm, which can be ascribed to the NBE PL emission and defect-related emission of  $\text{MA}_3\text{Bi}_2\text{Br}_9$ ,

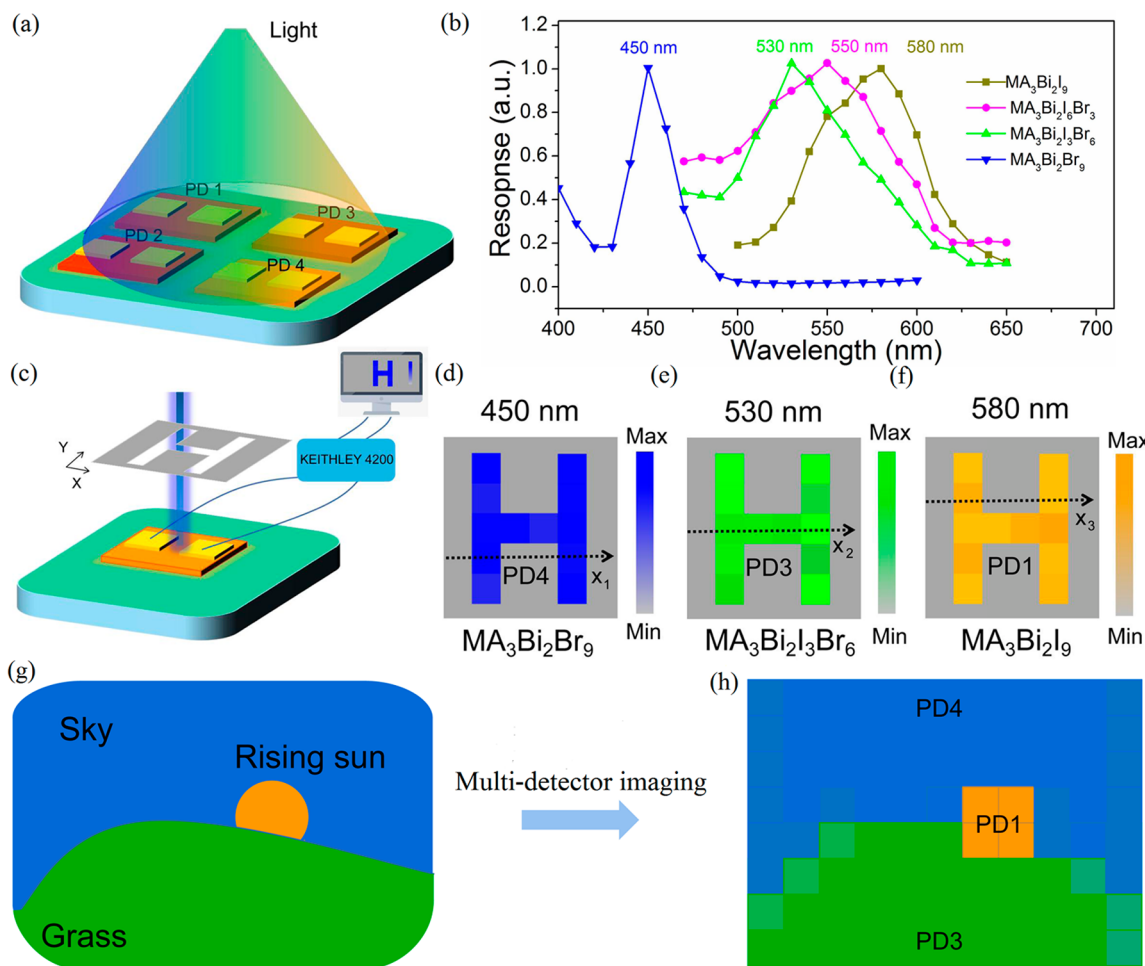


**Figure 4.** (a) Schematic and (b) corresponding normalized responsivity spectra of four types of PDs, namely, Au- $\text{MA}_3\text{Bi}_2\text{I}_9$ -Au (PD1), Au- $\text{MA}_3\text{Bi}_2\text{I}_6\text{Br}_3$ -Au (PD2), Au- $\text{MA}_3\text{Bi}_2\text{I}_3\text{Br}_6$ -Au (PD3), and Au- $\text{MA}_3\text{Bi}_2\text{Br}_9$ -Au (PD4). (c) Schematic of the imaging system employing the PDs as image pixels. (d–f) Imaging results obtained using different PDs under different lights. (g) Schematic of the light-sensing array. (h) Photocurrent mapping results under illumination of a specific light.

respectively.<sup>21</sup> The high-resolution TEM (HRTEM) image of  $\text{MA}_3\text{Bi}_2\text{I}_9$  exhibits clearly visible lattice stripes, and the interlayer spacing of 0.36 nm is attributed to the d spacing of the (003) crystal planes. The selected-area electron diffraction (SAED) pattern of  $\text{MA}_3\text{Bi}_2\text{I}_9$  exhibits obvious and periodic diffraction spots, indicating the high single crystallinity of  $\text{MA}_3\text{Bi}_2\text{I}_9$ .

To determine the energy band information on  $\text{MA}_3\text{Bi}_2\text{I}_{3x}\text{Br}_{9-3x}$  ( $x = 0, 1, 2$ , and 3) perovskites, DFT calculations were further performed. The crystal structures of  $\text{MA}_3\text{Bi}_2\text{I}_9$ ,  $\text{MA}_3\text{Bi}_2\text{I}_3\text{Br}_6$ , and  $\text{MA}_3\text{Bi}_2\text{Br}_9$  are shown in Figures 3a and S3, respectively. Based on the band structures (Figure 3b–d) and densities of states (DOSs) (Figure 3e–g), the band gaps of  $\text{MA}_3\text{Bi}_2\text{I}_9$ ,  $\text{MA}_3\text{Bi}_2\text{I}_3\text{Br}_6$ , and  $\text{MA}_3\text{Bi}_2\text{Br}_9$  increase with an increase in the Br atom ratio. Besides, parts b–d of Figure 3 show that  $\text{MA}_3\text{Bi}_2\text{I}_9$  and  $\text{MA}_3\text{Bi}_2\text{I}_3\text{Br}_6$  exhibit direct band gaps, whereas  $\text{MA}_3\text{Bi}_2\text{Br}_9$  exhibits an indirect band gap. The direct band gap of  $\text{MA}_3\text{Bi}_2\text{I}_9$  (7.2 mA W<sup>-1</sup>; 580 nm; 2 V) affords it with a better optical detection performance than that of  $\text{MA}_3\text{Bi}_2\text{Br}_9$  (1.5 mA W<sup>-1</sup>; 450 nm; 2 V), as shown in Figure S4. Additionally, the projected DOS exhibits that the valence band (VB) and conduction band (CB) are dominated by I and Bi bands in  $\text{MA}_3\text{Bi}_2\text{I}_9$ , I, Br, and Bi bands in  $\text{MA}_3\text{Bi}_2\text{I}_3\text{Br}_6$ , and Br and Bi bands in  $\text{MA}_3\text{Bi}_2\text{Br}_9$ . To further disclose the Fermi level ( $E_f$ ), the CB and VB positions of the microplates were

used. The VB spectrum (the energy band position relative to the Fermi level; Figure 3h), energy band spectrum (Figure 3i), and Kelvin probe force microscopy (KPFM; Figure 3j) spectra were further studied. The VB bands of  $\text{MA}_3\text{Bi}_2\text{I}_9$ ,  $\text{MA}_3\text{Bi}_2\text{I}_3\text{Br}_6$ ,  $\text{MA}_3\text{Bi}_2\text{I}_3\text{Br}_6$ , and  $\text{MA}_3\text{Bi}_2\text{Br}_9$  are 0.97, 1.24, 1.50, and 1.71 eV, respectively, showing an obvious increase with an increase of the Br contents. The optical band gaps of the microplates were determined using the equation<sup>25–27</sup>  $(ah\nu)^2 = A(\hbar\nu - E_g)$ , where  $\alpha$  is the absorption coefficient,  $\hbar\nu$  is the photon energy,  $A$  is the constant,  $n = 2$  for the direct-band-gap materials, and  $n = 0.5$  for the indirect-band-gap materials. The calculated band gaps of  $\text{MA}_3\text{Bi}_2\text{I}_9$ ,  $\text{MA}_3\text{Bi}_2\text{I}_3\text{Br}_6$ ,  $\text{MA}_3\text{Bi}_2\text{I}_3\text{Br}_6$ , and  $\text{MA}_3\text{Bi}_2\text{Br}_9$  are 2.06, 2.12, 2.25, and 2.55 eV, respectively. KPFM shows that  $E_f$  of  $\text{MA}_3\text{Bi}_2\text{I}_9$  is 5.14 eV and that of  $\text{MA}_3\text{Bi}_2\text{Br}_9$  is 4.93 eV. According to the above results, the CB and VB (the energy band position relative to vacuum) of  $\text{MA}_3\text{Bi}_2\text{I}_9$  are 4.05 and 6.11 eV and those of  $\text{MA}_3\text{Bi}_2\text{Br}_9$  are 4.09 and 6.64 eV, respectively, as shown in Figure 3k. Furthermore, it can be found that  $E_f$  of  $\text{MA}_3\text{Bi}_2\text{I}_9$  is close to the VB, whereas that of  $\text{MA}_3\text{Bi}_2\text{Br}_9$  is close to the CB; therefore,  $\text{MA}_3\text{Bi}_2\text{I}_9$  is a p-type semiconductor, and  $\text{MA}_3\text{Bi}_2\text{Br}_9$  is an n-type semiconductor. The band structure of  $\text{MA}_3\text{Bi}_2\text{I}_{3x}\text{Br}_{9-3x}$  ( $x = 0, 1, 2$ , and 3) perovskites will guide the future development of more efficient optoelectronic devices.

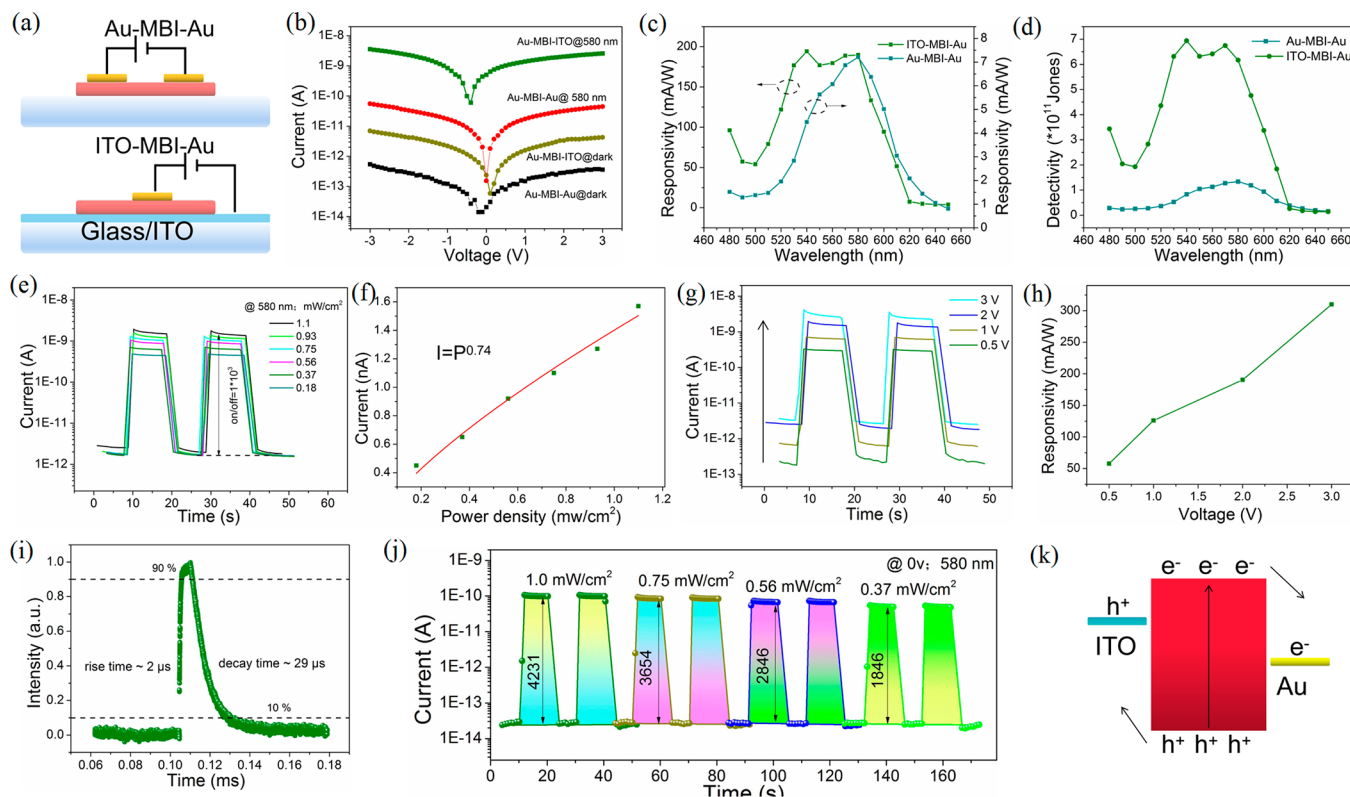


**Figure 5.** (a) Schematic of Au- $\text{MA}_3\text{Bi}_2\text{I}_9$ -Au and ITO- $\text{MA}_3\text{Bi}_2\text{I}_9$ -Au devices. (b–d) Corresponding  $I$ – $V$  curves, responsivity, and detectivity of the device in part a. (e)  $I$ – $T$  curves of ITO- $\text{MA}_3\text{Bi}_2\text{I}_9$ -Au under different light intensities at 580 nm and (f) corresponding fitting curves. (g)  $I$ – $T$  curves of ITO- $\text{MA}_3\text{Bi}_2\text{I}_9$ -Au under different voltages at 580 nm and (h) responsivity versus voltage. (i) Pulsed light response of the ITO- $\text{MA}_3\text{Bi}_2\text{I}_9$ -Au PD. (j)  $I$ – $T$  curves of ITO- $\text{MA}_3\text{Bi}_2\text{I}_9$ -Au measured at 0 V under different light intensities. (k) Schematic of the band alignment of ITO- $\text{MA}_3\text{Bi}_2\text{I}_9$ -Au.

The tuned band gap of  $\text{MA}_3\text{Bi}_2\text{I}_{3x}\text{Br}_{9-3x}$  ( $x = 0, 1, 2$ , and  $3$ ) perovskites can be well applied in the photoimaging area with color-sensing abilities (450–580 nm). The optical image of the representative PD4 is shown in Figure S5. The linear behavior of the  $I$ – $V$  curves of all PDs (Figure S6) tested under dark and light conditions indicates the ohmic contact between Au and  $\text{MA}_3\text{Bi}_2\text{I}_{3x}\text{Br}_{9-3x}$  ( $x = 0, 1, 2$ , and  $3$ ) perovskites. As shown in Figure 4a, when the four PDs based on  $\text{MA}_3\text{Bi}_2\text{I}_9$ ,  $\text{MA}_3\text{Bi}_2\text{I}_6\text{Br}_3$ ,  $\text{MA}_3\text{Bi}_2\text{I}_3\text{Br}_6$ , and  $\text{MA}_3\text{Bi}_2\text{Br}_9$  perovskites are illuminated by a wavelength of 400–650 nm,  $\text{MA}_3\text{Bi}_2\text{I}_9$ ,  $\text{MA}_3\text{Bi}_2\text{I}_3\text{Br}_6$ , and  $\text{MA}_3\text{Bi}_2\text{Br}_9$ -based PDs exhibit obvious color-sensing abilities with response peaks centered at 580 ( $0.56 \text{ mW cm}^{-2}$ ), 530 ( $0.50 \text{ mW cm}^{-2}$ ), and 450 nm ( $0.53 \text{ mW cm}^{-2}$ ), respectively, as shown in Figure 4b. If only PD1 responds to the incident light, the wavelength is  $\sim$ 580 nm. If both PD1 and PD2 respond to the incident light, the wavelength is 550–580 nm. If only PD2 responds to the incident light, the wavelength is  $\sim$ 550 nm. If both PD2 and PD3 respond to the incident light, the wavelength is 530–550 nm. If only PD3 responds to the incident light, the wavelength is  $\sim$ 530 nm. If both PD3 and PD4 respond to the incident light, the wavelength is 450–530 nm. If only PD4 responds to the incident light, the wavelength is  $\sim$ 450 nm. An imaging system was constructed after the color of the incident light was determined using the above PDs (Figure 4c). A hollow template with H graphics ( $2.5 \times 3 \text{ cm}$ ) was placed between the light and PDs. A Keithley 4200 semiconductor was used to analyze the optical signal while the template was continuously moved in X and Y directions, as shown in Figure 4c. The image “H” can be realized using different PDs, as shown in Figures 4d–f and S7d1–f1 (the

corresponding IT curves along the  $x_1$ ,  $x_2$ , and  $x_3$  lines).<sup>28</sup> Furthermore, light with shape and color as shown in Figure 4g are illuminated on PD1, PD3, and PD4, respectively. Different  $\text{MA}_3\text{Bi}_2\text{I}_{3x}\text{Br}_{9-3x}$  ( $x = 0, 1, 2$ , and  $3$ ) perovskites respond to light with different wavelengths (450, 530, and 580 nm), which can realize photoimaging with color-sensing abilities, as shown in Figure 4h.

The  $\text{MA}_3\text{Bi}_2\text{I}_9$  (MBI) sample was further selected to study the photodetecting abilities of MBI with horizontal (Au-MBI-Au; electronic transport channel =  $25 \mu\text{m}$ ) and vertical (Au-MBI-ITO; electronic transport channel =  $5.8 \mu\text{m}$ ) electrode structures, as shown in Figure 5a. The  $I$ – $V$  curves (Figure 5b) show that the two PDs are sensitive to 580 nm light. Au-MBI-ITO exhibits higher dark current than and considerably increased photocurrent compared to Au-MBI-Au because of the asymmetric electrodes and reduced electron-transport channels, which can accelerate electron–hole separation and reduce their consumption.  $R$  and  $D^*$  of both PDs are compared in Figure 5c,d. Both PDs show a peak  $R$  and  $D^*$  at  $\sim$ 580 nm, and the  $R$  and  $D^*$  of Au-MBI-ITO are  $189.8 \text{ mA W}^{-1}$  and  $6.2 \times 10^{11} \text{ Jones}$ , which is  $26.4$  ( $7.2 \text{ mA W}^{-1}$ ) and  $4.8$  ( $1.3 \times 10^{11}$ ) times those of Au-MBI-Au, respectively. Figure 5e shows the  $I$ – $T$  curves of the Au-MBI-ITO PD at different light intensities. The light current increases with an increase in the light intensities. When the light intensity increases to  $1.1 \text{ mW cm}^{-2}$ , an on/off ratio of  $1.02 \times 10^3$  is obtained. Figure 5f shows the dependence of the photocurrent on the light intensity ( $I_l = p^\theta$ , where  $0 < \theta < 1$ ; a large  $\theta$  means less defects in the PD). The value of  $\theta$  is 0.74 for Au-MBI-ITO PD, indicating the presence of less defects in the MBI crystal. Parts g and h of

Figure 5 show that the photocurrent and  $R$  increase with an increase in the photointensities, and the highest  $R$  of  $310.4 \text{ mA W}^{-1}$  is obtained at a  $3 \text{ V}$  bias ( $580 \text{ nm}$ ;  $0.56 \text{ mW cm}^{-2}$ ). The fast response speed is an important figure of merit for evaluating a PD. Figure 5i shows that the PD exhibits a fast rise and decay time, which are  $2$  and  $29 \mu\text{s}$ , respectively. The decay process of the PD was fitted by  $I = I_0 + A_1 e^{-t/\tau_1} + A_2 e^{-t/\tau_2}$ , where  $I_0$  is the steady-state photocurrent,  $t$  is the time,  $A_1$  and  $A_2$  are constants, and  $\tau_1$  and  $\tau_2$  are relaxation time constants. The fitted  $\tau_1 = 1.3 \mu\text{s}$  and  $\tau_2 = 7.6 \mu\text{s}$ , as shown in Figure S8. Usually, the fast-response component is due to a rapid change in the carrier concentration when light is turned off; the slow-response component is due to a carrier being released from defects. Self-powered PDs may have extensive application values. The photodetection ability of Au-MBI-ITO PD under a  $0 \text{ V}$  bias at different light intensities was studied (Figure 5j). The on/off ratio and photocurrent increase with an increase in the light intensity, and the highest on/off ratio is  $4231$  at a light intensity of  $1.0 \text{ mW cm}^{-2}$ . Moreover, the corresponding self-powered  $R$  and LDR are  $15.8 \text{ mA W}^{-1}$  and  $72.5 \text{ dB}$ , respectively. The performance of our PD is comparable or superior to that of most of the reported lead-free perovskite PDs, as shown in Table S1. The PD maintains  $80.3\%$  and  $63\%$  of its original photodetecting ability after  $1000$  cycles and  $15$  days under environmental conditions, respectively, as shown in Figure S9a ( $\sim 1000$  cycles,  $I-t$  test) and Figure S9b ( $I-T$  curves after  $15$  days). The potential difference between the Au and ITO electrodes affords the PD with a better self-powered performance. When the PD is illuminated by light, the photogenerated electrons and holes move to Au and ITO, respectively, under an electrode potential difference.<sup>29,30</sup>

## 4. CONCLUSIONS

In summary, single-crystal  $\text{MA}_3\text{Bi}_2\text{I}_{3x}\text{Br}_{9-3x}$  ( $x = 0, 1, 2$ , and  $3$ ) perovskites with color-sensing abilities ( $450$ – $580 \text{ nm}$ ) were systematically studied for the first time. The band structure exploration shows that  $\text{MA}_3\text{Bi}_2\text{I}_9$  is a p-type direct-band-gap semiconductor, whereas  $\text{MA}_3\text{Bi}_2\text{Br}_9$  is an n-type indirect-band-gap semiconductor. The energy band gap of  $\text{MA}_3\text{Bi}_2\text{I}_{3x}\text{Br}_{9-3x}$  ( $x = 0, 1, 2$ , and  $3$ ) perovskites can be tuned from  $2.06$  to  $2.55 \text{ eV}$ , which affords it color-sensing abilities from  $450$  to  $580 \text{ nm}$  with an increase in the I proportion. The Au- $\text{MA}_3\text{Bi}_2\text{I}_9$ -ITO PD exhibits a superior self-powered photodetecting performance with a high responsivity ( $15.8 \text{ mA W}^{-1}$ ;  $580 \text{ nm}$ ;  $1 \text{ mW cm}^{-2}$ ), detectivity ( $8.1 \times 10^{11} \text{ Jones}$ ), an on/off ratio ( $4231$ ), LDR ( $72.5 \text{ dB}$ ), and a fast response speed (rise time =  $2 \mu\text{s}$ ; decay time =  $29 \mu\text{s}$ ). This study not only is conducive to an in-depth understanding of perovskite materials but also provides great application prospects in object interaction and color perception.

## ■ ASSOCIATED CONTENT

### Supporting Information

The Supporting Information is available free of charge at <https://pubs.acs.org/doi/10.1021/acsami.3c03454>.

Additional characterizations (SEM mapping, XPS, crystal structure, responsivity, optical image,  $I-V$  curves, and  $I-T$  results) and supplementary tables and notes (PDF)

## ■ AUTHOR INFORMATION

### Corresponding Authors

Xiaosheng Fang – Department of Materials Science, State Key Laboratory of Molecular Engineering of Polymers Fudan University, Shanghai 200433, P. R. China;  [orcid.org/0000-0003-3387-4532](https://orcid.org/0000-0003-3387-4532); Email: [xshfang@fudan.edu.cn](mailto:xshfang@fudan.edu.cn)

Limin Wu – Department of Materials Science, State Key Laboratory of Molecular Engineering of Polymers Fudan University, Shanghai 200433, P. R. China; College of Chemistry and Chemical Engineering Inner Mongolia University, Hohhot 010021, P. R. China;  [orcid.org/0000-0001-8495-8627](https://orcid.org/0000-0001-8495-8627); Email: [lmw@fudan.edu.cn](mailto:lmw@fudan.edu.cn)

### Authors

Fa Cao – Department of Materials Science, State Key Laboratory of Molecular Engineering of Polymers Fudan University, Shanghai 200433, P. R. China

Xiaolei Deng – Department of Materials Science, State Key Laboratory of Molecular Engineering of Polymers Fudan University, Shanghai 200433, P. R. China

Xinya Liu – Department of Materials Science, State Key Laboratory of Molecular Engineering of Polymers Fudan University, Shanghai 200433, P. R. China

Li Su – Department of Materials Science, State Key Laboratory of Molecular Engineering of Polymers Fudan University, Shanghai 200433, P. R. China

Enliu Hong – Department of Materials Science, State Key Laboratory of Molecular Engineering of Polymers Fudan University, Shanghai 200433, P. R. China

Complete contact information is available at: <https://pubs.acs.org/10.1021/acsami.3c03454>

### Author Contributions

The manuscript was written through contributions of all authors. All authors have given approval to the final version of the manuscript.

### Notes

The authors declare no competing financial interest.

## ■ ACKNOWLEDGMENTS

This work is supported by National Natural Science Foundation of China (Nos. 92263106, 12061131009, and 12211530438), the China Postdoctoral Science Foundation (2022M710710), and Science and Technology Commission of Shanghai Municipality (Nos. 21520712600 and 19520744300).

## ■ REFERENCES

- (1) Lien, M.-B.; Liu, C.-H.; Chun, I. Y.; Ravishankar, S.; Nien, H.; Zhou, M.; Fessler, J. A.; Zhong, Z.; Norris, T. B. Ranging and Light Field Imaging with Transparent Photodetectors. *Nat. Photonics* **2020**, *14*, 143–148.
- (2) Zhang, X. N.; Liu, X. Y.; Sun, B.; Ye, H. B.; He, C. H.; Kong, L. X.; Li, G. L.; Liu, Z. Y.; Liao, G. L. Ultrafast, Self-Powered, and Charge-Transport-Layer-Free Ultraviolet Photodetectors Based on Sequentially Vacuum-Evaporated Lead-Free  $\text{Cs}_2\text{AgBiBr}_6$  Thin Films. *ACS Appl. Mater. Interface* **2021**, *13*, 35949–35960.
- (3) Li, S.; Zhang, Y.; Yang, W.; Liu, H.; Fang, X. S. 2D Perovskite  $\text{Sr}_2\text{Nb}_3\text{O}_{10}$  for High-Performance UV Photodetectors. *Adv. Mater.* **2020**, *32*, 1905443.
- (4) Wang, H. P.; Li, S.; Liu, X.; Shi, Z.; Fang, X. S.; He, J. H. Low-Dimensional Metal Halide Perovskite Photodetectors. *Adv. Mater.* **2021**, *33*, 2003309.

- (5) Chen, Y. H.; Su, L. X.; Jiang, M. M.; Fang, X. S. Switch Type PANI/ZnO Core-shell Microwire Heterojunction for UV Photodetection. *J. Mater. Sci. Technol.* **2022**, *105*, 259.
- (6) Cao, F.; Li, Z.; Liu, X.; Shi, Z.; Fang, X. S. Air Induced Formation of  $\text{Cs}_3\text{Bi}_2\text{Br}_9/\text{Cs}_3\text{BiBr}_6$  Bulk Heterojunction and Its Dual-Band Photodetection Abilities for Light Communication. *Adv. Funct. Mater.* **2022**, *32*, 2206151.
- (7) Cao, F.; Yan, T.; Li, Z.; Wu, L.; Fang, X. S. Dual-Band Perovskite Bulk Heterojunction Self-Powered Photodetector for Encrypted Communication and Imaging. *Adv. Opt. Mater.* **2022**, *10*, 2200786.
- (8) Ji, Z.; Liu, Y.; Zhao, C.; Wang, Z.; Mai, W. Perovskite Wide-Angle Field-Of-View Camera. *Adv. Mater.* **2022**, *34*, 2206957.
- (9) Sun, H.; Tian, W.; Wang, X.; Deng, K.; Xiong, J.; Li, L. In Situ Formed Gradient Bandgap-Tunable Perovskite for Ultrahigh-Speed Color/Spectrum-Sensitive Photodetectors Via Electron-Donor Control. *Adv. Mater.* **2020**, *32*, 1908108.
- (10) Fang, Y.; Dong, Q.; Shao, Y.; Yuan, Y.; Huang, J. Highly Narrowband Perovskite Single-Crystal Photodetectors Enabled by Surface-Charge Recombination. *Nat. Photonics* **2015**, *9*, 679–686.
- (11) Liu, Y.; Ji, Z.; Cen, G.; Sun, H.; Wang, H.; Zhao, C.; Wang, Z. L.; Mai, W. Perovskite-Based Color Camera Inspired by Human Visual Cells. *Light Sci. Appl.* **2023**, *12*. DOI: [10.1038/s41377-023-01072-y](https://doi.org/10.1038/s41377-023-01072-y).
- (12) Xiao, Z.; Song, Z.; Yan, Y. From Lead Halide Perovskites to Lead-Free Metal Halide Perovskites and Perovskite Derivatives. *Adv. Mater.* **2019**, *31*, 1803792.
- (13) Wu, C.; Zhang, Q.; Liu, G.; Zhang, Z.; Wang, D.; Qu, B.; Chen, Z.; Xiao, L. From Pb to Bi: A Promising Family of Pb-free Optoelectronic Materials and Devices. *Adv. Energy Mater.* **2020**, *10*, 1902496.
- (14) Hao, D.; Liu, D.; Shen, Y.; Shi, Q.; Huang, J. Air-Stable Self-Powered Photodetectors based on Lead-Free  $\text{CsBi}_3\text{I}_{10}/\text{SnO}_2$  Heterojunction for Weak Light Detection. *Adv. Funct. Mater.* **2021**, *31*, 2100773.
- (15) Tang, Y.; Mak, C. H.; Liu, R.; Wang, Z.; Ji, L.; Song, H.; Tan, C.; Barrière, F.; Hsu, H. Y. In Situ Formation of Bismuth-based Perovskite Heterostructures for High-Performance Cocatalyst-Free Photocatalytic Hydrogen Evolution. *Adv. Funct. Mater.* **2020**, *30*, 2006919.
- (16) Chen, X.; Jia, M.; Xu, W.; Pan, G.; Zhu, J.; Tian, Y.; Wu, D.; Li, X.; Shi, Z. Recent Progress and Challenges of Bismuth-Based Halide Perovskites for Emerging Optoelectronic Applications. *Adv. Opt. Mater.* **2023**, *11*, 2202153.
- (17) Cao, F.; Jin, L.; Wu, Y.; Ji, X. High-Performance, Self-Powered UV Photodetector Based on Au Nanoparticles Decorated ZnO/CuI Heterostructure. *J. Alloy. Compd.* **2021**, *859*, 158383.
- (18) Hohenberg, P.; Kohn, W. Inhomogeneous Electron Gas. *Phys. Rev.* **1964**, *136*, B864–B871.
- (19) Kresse, G.; Furthmüller, J. Efficient Iterative Schemes for ab Initio Total-Energy Calculations Using A Plane-Wave Basis Set. *Phys. Rev. B* **1996**, *54*, 11169–11186.
- (20) Perdew, J. P.; Burke, K.; Ernzerhof, M. Generalized Gradient Approximation Made Simple. *Phys. Rev. Lett.* **1996**, *77*, 3865–3868.
- (21) Leng, M.; Chen, Z.; Yang, Y.; Li, Z.; Zeng, K.; Li, K.; Niu, G.; He, Y.; Zhou, Q.; Tang, J. Lead-Free, Blue Emitting Bismuth Halide Perovskite Quantum Dots. *Angew. Chem., Int. Ed.* **2016**, *55*, 15012–15016.
- (22) Tang, Y.; Mak, C. H.; Zhang, J.; Jia, G.; Cheng, K. C.; Song, H.; Yuan, M.; Zhao, S.; Kai, J. J.; Colmenares, J. C.; Hsu, H. Y. Unravelling the Interfacial Dynamics of Band-Gap Funneling in Bismuth-Based Halide Perovskites. *Adv. Mater.* **2023**, *35*, 2207835.
- (23) Li, Q.; Yin, L.; Chen, Z.; Deng, K.; Luo, S.; Zou, B.; Wang, Z.; Tang, J.; Quan, Z. High Pressure Structural and Optical Properties of Two-Dimensional Hybrid Halide Perovskite  $(\text{CH}_3\text{NH}_3)_3\text{Bi}_2\text{Br}_9$ . *Inorg. Chem.* **2019**, *58*, 1621–1626.
- (24) Leng, M.; Yang, Y.; Chen, Z.; Gao, W.; Zhang, J.; Niu, G.; Li, D.; Song, H.; Zhang, J.; Jin, S.; Tang, J. Surface Passivation of Bismuth-Based Perovskite Variant Quantum Dots to Achieve Efficient Blue Emission. *Nano Lett.* **2018**, *18*, 6076–6083.
- (25) Cao, F.; Wang, T.; Ji, X. Enhanced Visible Photocatalytic Activity of Tree-Like ZnO/CuO Nanostructure on Cu Foam. *Appl. Surf. Sci.* **2019**, *471*, 417–424.
- (26) Meng, X.; Li, Z.; Zeng, H.; Chen, J.; Zhang, Z. MoS<sub>2</sub> Quantum Dots-Interspersed Bi<sub>2</sub>WO<sub>6</sub> Heterostructures for Visible Light-Induced Detoxification and Disinfection. *Appl. Catal. B: Environ.* **2017**, *210*, 160–172.
- (27) Cao, F.; Pan, Z.; Ji, X. An Approach For Fabrication of Micrometer Linear ZnO/Ti<sub>3</sub>C<sub>2</sub>T<sub>x</sub> UV photodetector with High Responsivity and EQE. *J. Appl. Phys.* **2021**, *129*, 204503.
- (28) Li, L.; Chen, H. Y.; Fang, Z. M.; Meng, X. Y.; Zuo, C. T.; Lv, M. L.; Tian, Y. Z.; Fang, Y.; Xiao, Z.; Shan, C. X.; Xiao, Z. G.; Jin, Z. W.; Shen, G. Z.; Shen, L.; Ding, L. M. An Electrically Modulated Single-Color/Dual-Color Imaging Photodetector. *Adv. Mater.* **2020**, *32*, 1907257.
- (29) Chen, J. C.; Liu, X. Y.; Li, Z. Q.; Cao, F.; Lu, X.; Fang, X. S. Work-Function-Tunable MXenes Electrodes to Optimize p-CsCu<sub>2</sub>I<sub>3</sub>/n-Ca<sub>2</sub>Nb<sub>3-x</sub>Ta<sub>x</sub>O<sub>10</sub> Junction Photodetectors for Image Sensing and Logic Electronics. *Adv. Funct. Mater.* **2022**, *32*, 2201066.
- (30) Li, W.; Liu, Y.; Gao, Y.; Ji, Z.; Fu, Y.; Zhao, C.; Mai, W. Tunneling-Assisted Highly Sensitive and Stable Lead-Free Cs<sub>3</sub>Bi<sub>2</sub>I<sub>9</sub> Perovskite Photodetectors for Diffuse Reflection Imaging. *J. Mater. Chem. C* **2021**, *9*, 1008–1013.

## Recommended by ACS

### Photoelectric Bi<sub>2</sub>S<sub>3</sub> Nanoparticle/Ti<sub>3</sub>C<sub>2</sub>T<sub>x</sub> Nanosheet Heterojunction for Promotion of Nerve Cell Growth

Fangwei Qi, Cijun Shuai, et al.

JULY 07, 2023

ACS APPLIED NANO MATERIALS

READ

### Elucidating the Role of Antimony Dopant in Optical Properties of Brightly Luminescent Zero-Dimensional Organic-Inorganic Metal Halides

Cheng Luo, Bin Yang, et al.

MAY 23, 2023

THE JOURNAL OF PHYSICAL CHEMISTRY C

READ

### Efficient Yellow Emission and Near-Unified Photoluminescence Quantum Yield of Sb<sup>3+</sup> in a One-Dimensional Confinement Cadmium Chloride Lattice

Tao Huang, Bingsuo Zou, et al.

MARCH 21, 2023

ACS APPLIED ELECTRONIC MATERIALS

READ

### Plasmonic Nb<sub>2</sub>CT<sub>x</sub> MXene-MAPbI<sub>3</sub> Heterostructure for Self-Powered Visible-NIR Photodiodes

Zhixiong Liu, Husam N. Alshareef, et al.

MAY 01, 2022

ACS NANO

READ

Get More Suggestions >